Real-time, high-resolution x-ray diffraction measurements on shocked crystals at a synchrotron facility

Y. M. Gupta, Stefan J. Turneaure, K. Perkins, K. Zimmerman, N. Arganbright et al.

Related Articles

Interferometric hard x-ray phase contrast imaging at 204 nm grating period
Rev. Sci. Instrum. 84, 013706 (2013)

Single-order operation of lamellar multilayer gratings in the soft x-ray spectral range
AIP Advances 3, 012103 (2013)

Spatial resolution of synchrotron x-ray microtomography in high energy range: Effect of x-ray energy and sample-to-detector distance
Appl. Phys. Lett. 101, 261901 (2012)

Formation of native defects in the γ-ray detector material Cs2Hg6S7
Appl. Phys. Lett. 101, 202103 (2012)

Integration of a broad beam ion source with a high-temperature x-ray diffraction vacuum chamber
Rev. Sci. Instrum. 83, 113901 (2012)

Additional information on Rev. Sci. Instrum.

Real-time, high-resolution x-ray diffraction measurements on shocked crystals at a synchrotron facility

Y. M. Gupta,[1] Stefan J. Turneaure,[1] K. Perkins,[1] K. Zimmerman,[1] N. Arganbright,[1] G. Shen,[2] and P. Chow[2]

[1]*Institute for Shock Physics and the Department of Physics, Washington State University, Pullman, Washington 99164-2816, USA*
[2]*HPCAT, Geophysical Laboratory, Carnegie Institution of Washington, Argonne, Illinois 60437, USA*

The Advanced Photon Source (APS) at Argonne National Laboratory was used to obtain real-time, high-resolution x-ray diffraction measurements to determine the microscopic response of shock-compressed single crystals. Disk shaped samples were subjected to plane shock wave compression by impacting them with half-inch diameter, flat-faced projectiles. The projectiles were accelerated to velocities ranging between 300 and 1200 m/s using a compact powder gun designed specifically for use at a synchrotron facility. The experiments were designed to keep the sample probed volume under uniaxial strain and constant stress for a duration longer than the 153.4 ns spacing between x-ray bunches. X-rays from a single pulse (<100 ps duration) out of the periodic x-ray pulses emitted by the synchrotron were used for the diffraction measurements. A synchronization and x-ray detection technique was developed to ensure that the measured signal was obtained unambiguously from the desired x-ray pulse incident on the sample while the sample was in a constant uniaxial strain state. The synchronization and x-ray detection techniques described can be used for a variety of x-ray measurements on shock compressed solids and liquids at the APS. Detailed procedures for applying the Bragg-Brentano parafocusing approach to single crystals at the APS are presented. Analytic developments to determine the effects of crystal substructure and non-ideal geometry on the diffraction pattern position and shape are presented. Representative real-time x-ray diffraction data, indicating shock-induced microstructural changes, are presented for a shock-compressed Al(111) sample. The experimental developments presented here provided, in part, the impetus for the Dynamic Compression Sector (DCS) currently under development at the APS. Both the synchronization/x-ray detection methods and the analysis equations for high-resolution single crystal x-ray diffraction can be used at the DCS. © *2012 American Institute of Physics*. [http://dx.doi.org/10.1063/1.4772577]

I. INTRODUCTION

A detailed understanding of shock wave induced changes in condensed systems requires real-time measurements at length scales ranging from the continuum level down to the atomic level.[1] At the crystal lattice scale, x-ray diffraction (XRD) measurements have been useful for gaining insight into shock-compressed solids.[2–20] Because of the short duration of shock wave experiments, typically sub-μs, intense x-ray sources are required for real-time examination of shock-compressed solids. Most shock compression experiments incorporating x-ray diffraction have been conducted using flash x-ray sources[2–13] or laser-based x-ray sources.[14–18] These x-ray sources provide relatively non-directional, characteristic x-rays, limiting both the types of experiments that can be performed and the resolution achievable in those experiments. In contrast, modern synchrotron x-ray sources are flexible, provide a highly collimated beam, tunable x-ray energy, bandwidths ranging from sub-eV to broadband, sub-nanosecond pulse durations, and a variety of temporal x-ray bunch spacings. Recently, synchrotron x-rays at the Advanced Photon Source (APS) have been used to examine solids shock compressed with both a powder gun[19,20] and a light gas gun.[21,22] High-resolution diffraction measurements have been made on single crystals[19,20] using monochromatic x-rays.

Imaging[21,22] and Laue diffraction[22] measurements have been obtained using a white beam. Synchrotron Laue diffraction measurements have also been reported for laser shocked single crystals.[23]

To routinely and optimally use synchrotron x-rays for diffraction, scattering, and x-ray imaging measurements in dynamic compression experiments, a dedicated experimental facility, termed the Dynamic Compression Sector (DCS), is currently under development at the Advanced Photon Source (Argonne National Laboratory, IL). The present article describes experimental developments successfully implemented at the APS[19,20] that demonstrated the feasibility of using modern synchrotrons for impact experiments. In particular, we describe experimental methods and analysis procedures for how the Bragg-Brentano parafocusing geometry was used at a synchrotron to examine the microstructural details of shock-compressed single crystals[19] and the strength of shocked and released crystals.[20]

An overview of the compact plate impact facility developed for use at a synchrotron and methods to interface the same to the synchrotron are presented in Sec. II. A key feature of our experimental design was the ability to unambiguously isolate the diffracted x-rays from a single x-ray pulse incident on the sample while it was in the desired constant
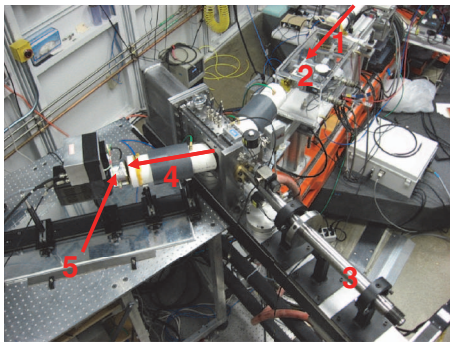
83, 123905-1

FIG. 1. Photograph of the experimental setup in hutch 16ID-D at HPCAT at the Advanced Photon Source showing the following items: (1) incident beam path, (2) horizontal focusing x-ray mirror, (3) powder gun, (4) diffracted beam path, and (5) x-ray detector.

uniaxial strain state. The x-ray detection, synchronization, and gating methods used to isolate the desired x-ray pulse are presented in Sec. III. Implementation of the Bragg-Brentano parafocusing geometry for shock-compressed single crystals[4] at a synchrotron source is described in Sec. IV. Particular attention is given to the relation between crystal microstructure and the diffraction pattern shape. Representative diffraction results are presented for both ambient and shock-compressed samples in Sec. V. Concluding remarks are summarized in Sec. VI.

II. EXPERIMENTAL SETUP

A. Hutch layout

The experimental setup, located in hutch 16ID-D at HP-CAT at the APS, is shown in Figure 1. The properties of the x-ray beam incident on the sample may be tuned for a particular experiment by varying the undulator insertion device settings and/or the beamline optics. The specific x-ray optics and geometry used in the present work are described in Sec. IV. The x-ray beam enters and exits the target chamber (see Fig. 2) through Lexan windows located on opposite sides
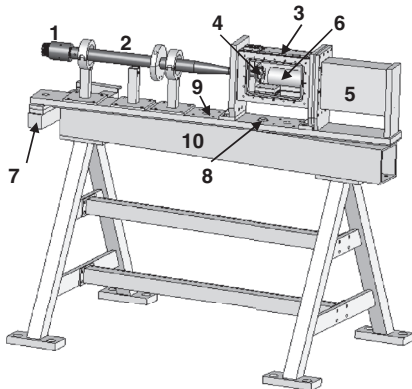

FIG. 2. Drawing of compact powder gun showing the following components: (1) breech, (2) half-inch bore and 3 ft long barrel, (3) target chamber, (4) target holder, (5) catch tank, (6) catch tube, (7) computer controlled driver for angle adjustment, (8) pivot point for gun rotation, (9) gun base plate, and (10) main gun support. The side flange of the target chamber is not shown on the incident beam side.
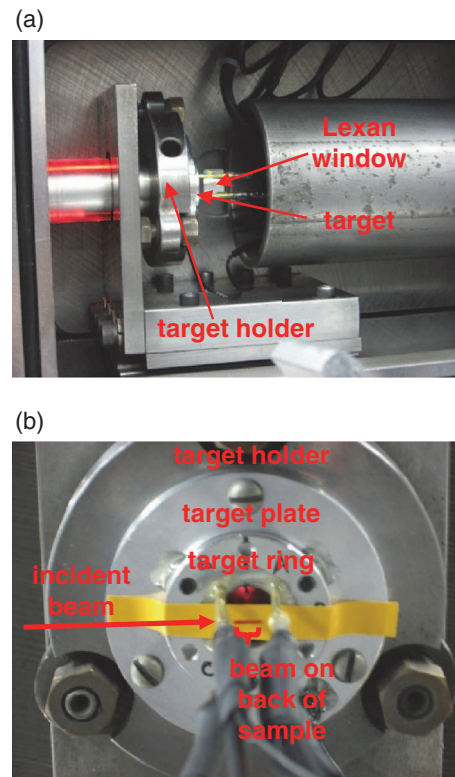

FIG. 3. Photographs of a target mounted inside the target chamber. (a) Side view of the target holder from the x-ray source side of the gun. The red lines above and below the barrel to the left of the target holder are due to light scatter from the laser diode beams used for projectile velocity measurement. (b) Target viewed from the back of the target holder. The line indicated in the figure shows where the x-ray beam was incident on the rear surface of a LiF sample as measured using burn paper.

of the target chamber (see Fig. 3(a)). A rectangular detector table with a breadboard top is located parallel and adjacent to the main gun support as shown in Fig. 1; the x-ray area detector was mounted on a rail whose position and angle were adjusted, for each experiment, to the desired settings relative to the edges of the detector table. Because the only mechanical coupling between the compact powder gun assembly and the detector and x-ray optics is through the floor, the detector and x-ray optics were not perturbed by the projectile launch.

B. Compact powder gun

The powder gun operating principles are similar to those of the gun described in Ref. 4. However, the present powder gun is smaller and was designed specifically for use at a synchrotron. The overall footprint of the gun is 66 in. × 40 in., allowing it to fit into the small confines of a typical synchrotron hutch. The gun barrel has a half-inch bore and is 3 ft long. Disk shaped samples were mounted about half an inch past the end of the gun barrel in the 15 in. long × 4.5 in. wide target chamber. Because the target chamber was narrow, an x-ray area detector placed alongside the chamber can cover a large solid angle relative to the center of the sample rear surface. This is particularly important for powder diffraction or Laue diffraction techniques. The projectile velocity was measured using a method similar to that described in Ref. 4.

Because the synchrotron beam direction is nearly fixed, the gun was designed to be mobile and flexible in its positioning relative to the beam. The following procedures were used to ensure a rapid setup of the gun/sample with respect to the synchrotron x-ray beam. The gun assembly was first moved (approximately) to the desired position and orientation with respect to the incident beam. The target holder height was designed to be nominally at the height of the monochromatic incident beam (~1.4 m). The target height was fine-tuned by adjusting four threaded feet at the ends of the A-frame gun supports until the incident beam was vertically centered on the sample. A manual dovetail translation stage (not shown in Fig. 2), located between the A-frame supports and the main gun support, was used to translate the target along the gun axis until the back of the target (located above the gun pivot point) was horizontally centered on the incident beam. For each experiment, both the translation and beam/sample angle were fine-tuned. The target holder was translated along the gun axis using a dovetail track inside the target chamber to position the back of the sample directly above the gun rotation pivot point. Finally, the incident beam/sample angle was set by rotating the gun and the gun base plate about the pivot point using a computer controlled Parker-Hannifin driver. The total range of angle adjustment was ±5° and the angular resolution was 0.01°. Figure 3(b) shows the incident x-ray beam striking the sample after the target alignment procedure was completed.

Projectile velocities from 300 to 1200 m/s could be obtained using either 2 or 3 in. long half-inch diameter Al projectiles and commercially available primers, cartridges, and gun powder. Using lighter projectiles, higher velocities are feasible. The launch was initiated by a solenoid striker (Physics Applications Inc.), which impacted a primer at the back of the cartridge. The delay time from the solenoid striker trigger signal to the projectile/target impact was 34 ms with about 1 ms jitter. The measured projectile velocities were typically within 2% of the desired velocities. The average tilt between the projectile and target at impact was 0.88 mrad with a standard deviation of 0.42 mrad. It was inferred from some of the x-ray diffraction results that the target might translate a distance t_{launch} (<30 μm) toward the gun barrel between launch initiation and impact. As described in Sec. IV, this translation can be corrected for when increased accuracy of the diffraction pattern shifts is needed.

C. Targets

Typical pictures of a target mounted in the target chamber are shown in Fig. 3, and a schematic side view of an impactor and target is shown in Fig. 4. The impact face of the target consisted of a 10 mm diameter, 2 mm thick z-cut quartz disk, and four concentrically placed piezoelectric PZT pins (Dynasen Inc.). The pins provide a trigger signal for the x-ray detection mechanism, and their relative impact times are used to determine the impact tilt.[4] To accommodate a 10 mm diameter target, it was necessary that the half-inch diameter impactor not strike the full diameter of the piezoelectric pins. The PZT pins provided adequate signal levels despite not being fully impacted. The purpose of the z-cut quartz buffers
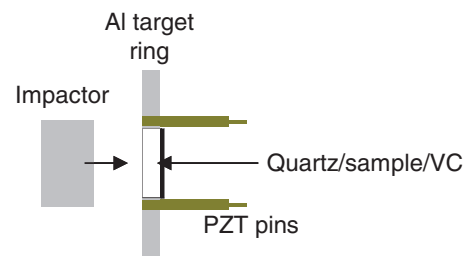

FIG. 4. Side schematic view of impactor and target.

was to delay the shock wave from reaching the back of the sample sufficiently for the x-ray detector to be gated on as described in Sec. III. The samples were bonded to the back of the quartz. In some of the experiments a vitreous carbon (VC) window was also bonded to the back of the sample.

III. X-RAY DETECTION: SYNCHRONIZATION WITH THE IMPACT EVENT

The common APS operation results in 24 equally spaced bunches in the storage ring producing periodic x-ray pulses (153.4 ns separation). Each pulse is less than 100 ps in duration. The timing and gating methods described below were designed for this mode of operation.

Time zero is defined as the moment the projectile impacts the target; it is uncorrelated to the phase of the x-ray pulses (see Fig. 5). The experiments were designed to have a shock wave time window from $t_{sw\ start}$ to $t_{sw\ end}$ during which the region of the sample exposed to the x-ray beam was subjected to macroscopic uniaxial strain; the stress state in the sample was nominally constant. In Fig. 5, the shock wave time window duration is shown as 153.4 ns. In practice, the thicknesses and diameters of the target pieces were chosen to provide somewhat longer shock wave time window durations. Thus, at least one x-ray pulse will arrive at the sample during the shock wave time window, although the exact arrival time of that x-ray pulse relative to the shock wave time window is unknown prior to the impact event. Many other x-ray pulses are also incident on the sample and detector both prior to and after the shock wave time window. It was desired to detect the diffracted x-rays from a single pulse, arriving at the sample during the shock wave time window, and to avoid detecting the signals from other x-ray pulses. To accomplish this, two criteria must be met: (1) the detector must be able to gate on and off faster than the 153.4 ns x-ray period and (2) the detector must be gated on and off for the desired x-ray bunch.

Our detection system consisted of the following components: a P47 phosphor (Y_2SiO_5:Ce) coated onto a fiber faceplate by Beam Imaging Solutions Inc., a microchannel plate (MCP) image intensifier (Photek), and a Princeton Instruments charge-coupled device with 20 μm pixel size. The detector was gated by biasing the MCP photocathode voltage on or off with a fast power supply (GBS Micro Power Supply). Gate rise and fall times of about 25 ns were achieved.

The P47 phosphor was essential to fast gating and was chosen because of its short decay time.[24] The use of P47 is uncommon in x-ray detection, though it has been previously
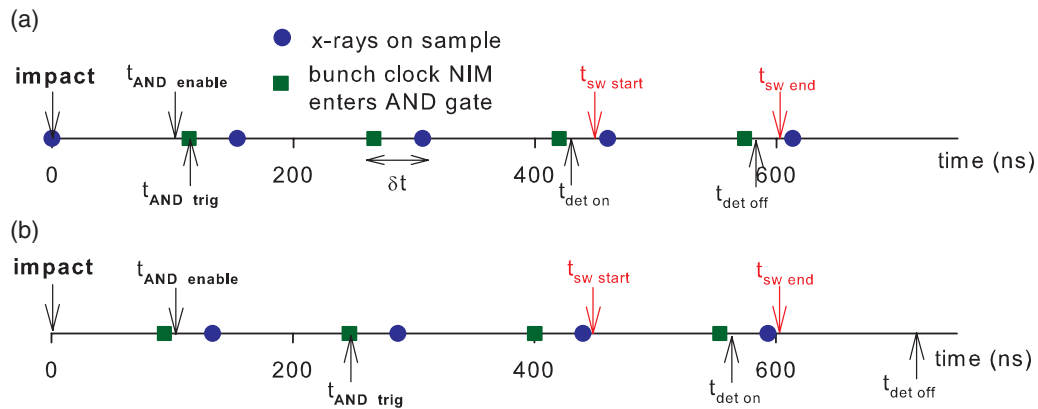
FIG. 5. Simplified timeline of events during a shock-wave experiment. Time zero is defined as the impact time. The shock wave time window beginning at $t_{sw\ start}$ and ending at $t_{sw\ end}$ is the time during which the rear sample surface, exposed to x-rays, is in a uniaxial strain constant stress state. In (a) the desired x-ray pulse arrives near the beginning of the time window, and in (b) the desired x-ray pulse arrives near the end of the time window. The x-ray detector is gated on between the times $t_{det\ on}$ and $t_{det\ off}$.

used in a fast x-ray camera.[25] Several tests were performed to determine the suitability of P47 for synchrotron shock-compression experiments. The dependence of light emitted from P47 was measured as a function of the P47 areal density for densities of 11, 15, and 20 mg/cm^2 with both 8 keV and 17.5 keV x-rays. The 20 mg/cm^2 phosphor had the greatest sensitivity at both x-ray energies; furthermore, the spatial resolutions were independent of the P47 areal density. Figure 6 shows the calculated fraction of incident x-rays absorbed by a 20 mg/cm^2 coating of P47 phosphor. The calculation was carried out using x-ray absorption values from Ref. 26. A 20 mg/cm^2 coating of P47 has a reasonable fraction of absorbed x-rays over a range of energies making it potentially useful for a variety of x-ray applications.

The temporal response of the detector was determined by measuring the light emitted from the P47 phosphor as a function of the detector gate on time relative to the x-ray pulse time (see Fig. 7). An exponential decay time of 48 ns was determined from a fit to the data. This is a reasonably short decay time compared with the 153.4 ns x-ray period. The signal level from the desired x-ray pulse will be more than 20 times larger than the signal level from the preceding x-ray
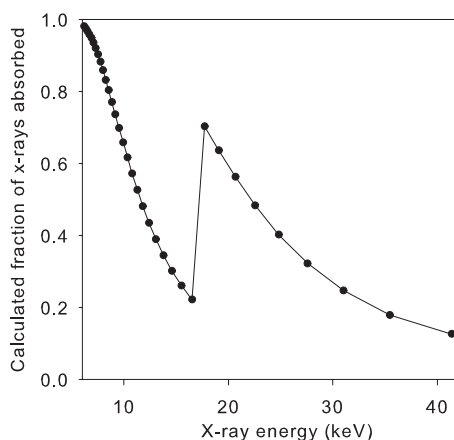
pulse (provided that the sample's diffraction properties do not change significantly as a result of shock compression between the arrivals of the two pulses).

The effects of both long-time P47 phosphor afterglow and imperfect MCP gating on the detected signal were examined. Each could potentially lead to an accumulation of signal from the thousands of pulses arriving at the detector before the impact event. The P47 phosphor afterglow signal was found to be less than 1% of the signal from a single pulse. The on/off gain ratio of the MCP was measured to be greater than 10^9. Even though the signals from the phosphor afterglow and the MCP bleed-through were determined to be relatively small compared to the signal from the desired single pulse, a millisecond shutter (Vincent Associates) was used to limit the x-ray exposure to about 15 ms. The shutter was opened about 25 ms after launch initiation and it was closed within several
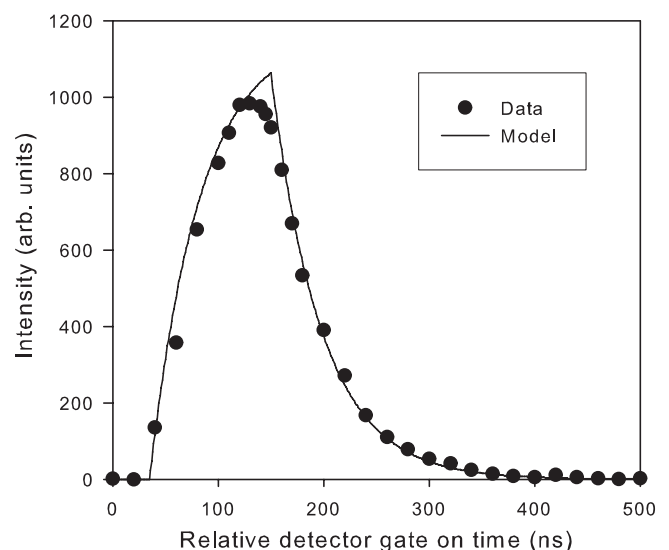
FIG. 7. Measured intensity from a single x-ray pulse as a function of the relative time at which the detector was gated on. For these measurements, the x-ray pulse was separated temporally from the next nearest pulse by over 1.59 μs. The gate pulse to the detector was 100 ns in duration. The model assumes a pure exponential decay of the P47 phosphor with a 48 ns time constant.

FIG. 6. Calculated fraction of incident x-rays absorbed for a 20 mg/cm^2 coating of P47 phosphor as a function of x-ray energy.

FIG. 8. Flowchart of signals and equipment used to gate the x-ray area detector.

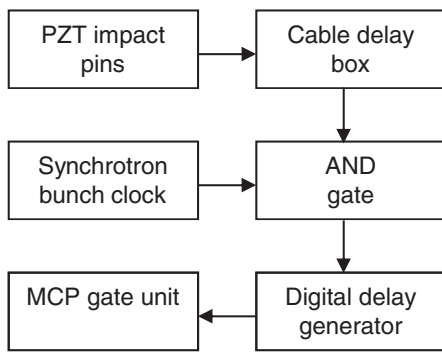FIG. 9. Schematic of the diffraction geometry used for high-resolution measurements of a single Bragg peak for a single crystal.

milliseconds of impact. In summary, the x-ray gating and detection method described above proved adequate for single pulse detection in the 24 bunch operation mode at the APS.

The method used to ensure that the single detected x-ray pulse arrived at the sample during the shock wave time window is summarized next. A flowchart of the equipment used to gate the detector to on is shown in Fig. 8. The signals from the four piezoelectric pins were combined with diode boxes and delayed by an adjustable cable delay box before entering an AND gate. The signal from the first pin to be impacted enabled the AND gate. Nuclear instrumentation module (NIM) pulses from the Advanced Photon Source's bunch clock entered the AND gate every 153.4 ns. Following the enabling of the AND gate, the next NIM pulse to enter the AND gate caused the AND gate to generate a transistor-transistor logic (TTL) pulse. This TTL pulse triggered an SRS DG535 digital delay generator which then provided a pulse that was used to gate the MCP on and off. The delay and the pulse length settings of the SRS DG535 were chosen such that the detector was gated on just before the arrival of an x-ray pulse at the detector and gated off just before the arrival of the next x-ray pulse. To ensure that the detector is gated on for the desired pulse, the following relation must be satisfied:

$$t_{sw\ start} - t_{AND\ enable} = N \times 153.4 ns + \delta t. \quad (1)$$

In relation (1), N is a positive integer and δt is the time difference between the x-ray pulses arriving at the sample and the bunch clock NIM signals arriving at the AND gate. The value of δt can be adjusted by delaying the bunch clock NIM signal and, in practice, it was adjusted such that $\delta t = 0$. For each experiment, the delay of the cable delay box in Fig. 8 was adjusted such that relation (1) was satisfied for $N = 2$. A minimum value of 2 was required for N because of the magnitude of the insertion delays between the NIM signal entering the AND gate and the detector gating on. Figure 5 shows that the detector is gated to on for the desired pulse in the two bounding cases where the desired pulse arrives at the beginning (Fig. 5(a)) or at the end (Fig. 5(b)) of a 153.4 ns duration shock wave time window. If relation (1) is not satisfied, the detector may gate on for any one of three x-ray pulses: the pulse prior to the desired one, the desired pulse, or the pulse arriving after the desired pulse. We performed 25 shock wave experiments using this synchronization approach;
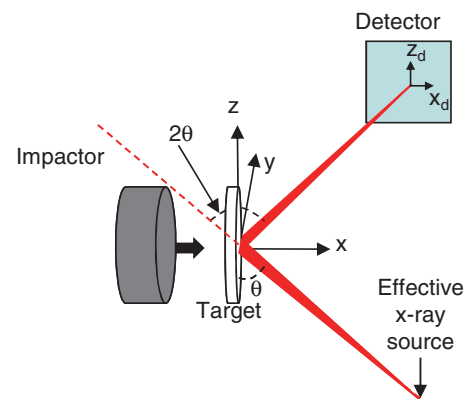
for all of these experiments, the detector was gated on for the desired pulse during the shock wave time window.

IV. X-RAY DIFFRACTION MEASUREMENT: BRAGG-BRENTANO PARAFOCUSING

A. Overview

The experimental arrangement used to examine a single Bragg peak of a shock-compressed single crystal is shown schematically in Fig. 9. The Bragg-Brentano parafocusing technique is very similar (in the horizontal plane) to the method described in Refs. 3 and 4. The incident x-rays diverge horizontally from an effective source (x-y plane) toward the single crystal sample over a range of angles, $\Delta\theta_{inc}$. The center of the sample's rear surface is located at a distance R_s from the effective x-ray source. The beam/sample angle is adjusted such that the Bragg condition

$$n\lambda = 2d_{hkl}\sin\theta \quad (2)$$

is satisfied near the center of the incident x-ray fan. In Eq. (2), n is the diffraction order, λ is the x-ray wavelength, d_{hkl} is the lattice spacing for the set of hkl lattice planes (normal to the loading direction) under investigation, and θ is the Bragg angle. A measurement of θ provides the lattice spacing, d_{hkl}. As in the earlier work,[3,4] the detector is located at a distance R_d (nominally equal to R_s) from the sample. The normal to the detector face nominally makes an angle θ_0 (the Bragg angle under ambient conditions) with the sample surface. The present work differs from the earlier work[3,4] in that the incident x-ray beam is more monochromatic, has a smaller effective source size, and is nearly collimated in the vertical direction. These differences result in higher resolution diffraction patterns, which provide more information about the crystal microstructure. Details of how the diffraction pattern shape relates to the crystal microstructure are described in Sec. IV C. The following effects, classifiable as instrumental broadening, are not included in the description of the diffraction pattern shape: finite x-ray bandwidth, finite x-ray source size, x-ray penetration into the sample, and detector resolution. Furthermore, broadening of the diffraction patterns due to size broadening effects (small coherently diffracting domains) is not considered. Methods used to account for

instrumental broadening and the size effect on diffraction pattern shape are described in Ref. 11. Before describing the XRD geometry in detail, we explain how the effective x-ray source was generated.

B. Effective x-ray source

The effective x-ray source was obtained as follows. The undulator A insertion device (3.3 cm period), located in the synchrotron storage ring, was tuned to produce a fundamental x-ray energy of about 8.8 keV. A double diamond crystal monochromator was used to reduce the bandwidth of the 8.8 keV x-rays to approximately 1 eV. The x-ray beam following the monochromator was nearly collimated and Kirkpatrick-Baez (KB) mirrors were used to focus the beam both vertically and horizontally. A 1 m long Rh coated mirror located about 8 m upstream of the sample and 57 m downstream from the center of the undulator source was used for vertical focusing. The location of the vertical focus was roughly 2 m upstream of the sample. The full width vertical divergence of the beam emanating from the vertical focal point was less than 0.01° and the beam height on the sample was approximately 250 μm. A 0.2 m long Rh coated mirror located about 0.6 m upstream from the sample and about 64 m downstream from the center of the undulator source was used for horizontal focusing. The location of the $\sim$30 μm wide horizontal focus defining the effective x-ray source position was $R_s = 0.4$ m upstream of the sample. The horizontal divergence angle of the incident beam from the effective x-ray source, $\Delta\theta_{inc}$, may be varied from near zero to several tenths of a degree by adjusting the horizontally focusing KB mirror. The width of the x-ray beam projected onto the sample depends on the Bragg angle θ_0 of the peak under examination, the beam divergence $\Delta\theta_{inc}$ and the value of R_s. For $\Delta\theta_{inc} = 0.2°$, $R_s = 0.4$ m, and a Bragg angle of 17.55° (corresponding to the Al 111 peak discussed later in the article), the x-ray beam diverging from the effective x-ray source covers a 4.6 mm wide region across the sample similar to what is shown in Fig. 3(b). Figure 10(a) shows a profile of the diverging beam ($\Delta\theta_{inc} = 0.2°$) measured with a single x-ray pulse that contained about 2×10^5 x-ray photons. A vertically binned cross section of the image is shown in Fig. 10(b). Except near the edges of the cross section, the angular distribution of intensity is reasonably smooth.

C. XRD geometry and experimental procedure

Because the synchrotron diffraction measurements have high resolution, it is worthwhile to consider the diffraction geometry in detail; deviations from an ideal geometry can affect the position and shape of the diffraction pattern. An ideal sample is defined as a non-mosaic single crystal with the hkl reciprocal lattice vector of interest normal to the sample face, i.e., along the x-axis. However, in practice, the hkl lattice planes may be somewhat misoriented with respect to the sample surface. In this case, the lattice will have components of rotation about the y- and z-axes with amplitudes of $\delta\theta_{mis,y}$ and $\delta\theta_{mis,z}$, respectively. A real sample may also be
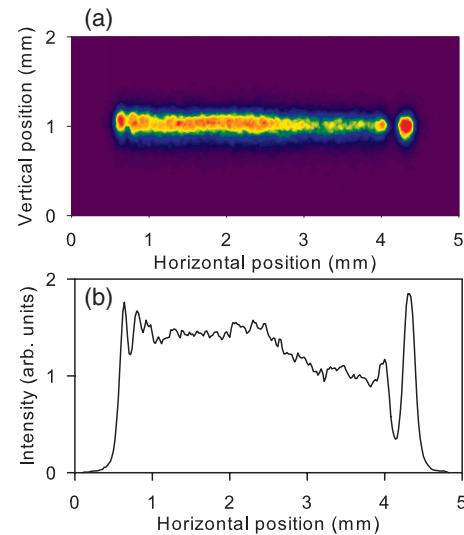

FIG. 10. (a) Image of horizontally diverging beam taken with a single pulse using the gated x-ray area detector. The detector was nominally perpendicular to the x-ray beam and the distance from the horizontal focus to the detector was 1.1 m. (b) Cross section of the diverging beam averaged vertically with the background subtracted.

somewhat mosaic and have a distribution of micro-lattice rotations about the y- and z-axes with position dependent amplitudes of $\delta\theta_{mos,y}$ and $\delta\theta_{mos,z}$, respectively. The net components of lattice rotation with respect to an ideally oriented sample are

$$\delta\theta_{m,y} = \delta\theta_{mis,y} + \delta\theta_{mos,y} \tag{3}$$

and

$$\delta\theta_{m,z} = \delta\theta_{mis,z} + \delta\theta_{mos,z}. \tag{4}$$

For the actual experiments, the axis of macroscopic misorientation was determined and the sample was oriented in the gun such that $\delta\theta_{mis,z}$ was nominally zero.

The following procedures were used to orient a sample with respect to the beam prior to a shock experiment. A PIN diode was used to measure the diffracted intensity as a function of the incident beam/sample angle; the beam/sample angle was then set to the central angle of the measured peak. As shown in Fig. 11(a), this corresponds to an angle of $\theta_0 - \delta\theta_{mis,z}$ between the center of the incident beam fan and the sample rear surface, where θ_0 is the ambient Bragg angle of the hkl peak being examined. Next, a reference diffraction pattern was obtained from the ambient crystal. The horizontal and vertical positions of this peak on the detector were defined as $x_d = 0$ and $z_d = 0$, respectively. The gun and sample were then rotated by an angle $\theta_{1e} - \theta_0$, which is the expected difference in the Bragg angle between the shocked and ambient states (see Fig. 11(b)). Both the incident x-ray beam and the detector remained stationary. If the pivot point for the gun rotation is not directly under the center of the sample, then the sample, in addition to being rotated, will be translated somewhat along the x- and y-axes. A small translation of the sample along the y-axis is unimportant because it will not change the relative position of the sample/beam intersection and the detector. However, a translation along the x-axis, t_{pivot}, must

(a) geometry for ambient reference

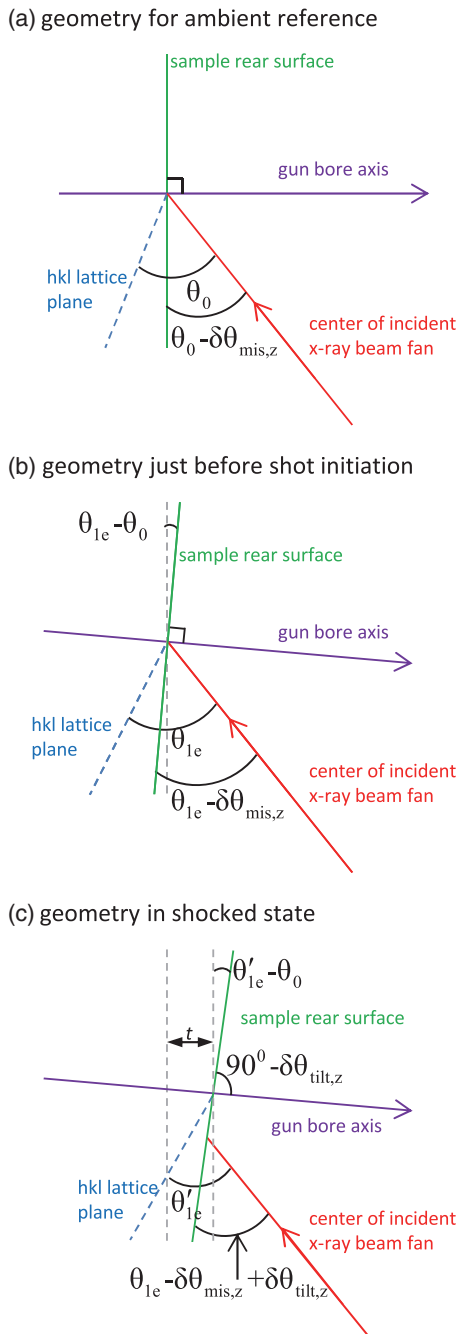(b) geometry just before shot initiation

(c) geometry in shocked state

FIG. 11. Horizontal plane (x-y) geometry of incident x-ray beam, sample rear surface, and the hkl lattice plane under investigation. (a) The geometry used when obtaining a reference diffraction pattern from the ambient crystal. (b) The geometry just prior to shot initiation after rotating the sample and gun such that the center of the incident x-ray beam fan will satisfy the Bragg condition for the expected lattice compression in the shocked state. (c) The geometry during the x-ray diffraction measurement of the shocked crystal.

be considered in determining the horizontal position of the peak on the detector.

As shown in Fig. 11(c), the projectile launch and the impact event result in additional geometry changes prior to the XRD measurement. The projectile tilt with respect to the target impact surface will rotate the crystal lattice about the y- and z-axes with components of amplitude $\delta\theta_{\text{tilt,y}}$ and $\delta\theta_{\text{tilt,z}}$, respectively.[3,4] The net rotation of the crystal about the z-axis

relative to the ambient state is then

$$\theta'_{1e} - \theta_0 = \theta_{1e} - \theta_0 + \delta\theta_{\text{tilt,z}}. \tag{5}$$

The actual Bragg angle in the shocked state (θ_1) may be somewhat different from θ'_{1e} because of projectile tilt ($\delta\theta_{\text{tilt,z}}$) and/or a difference between the actual (θ_1) and expected (θ_{1e}) Bragg angles. The horizontal divergence of the incident beam ($\Delta\theta_{\text{inc}} = 0.2°$) was chosen to accommodate the expected magnitude of these effects and still satisfy the Bragg condition somewhere in the incident fan of x-rays, even for a non-mosaic sample. The sample has an additional translation t_{shock} along the x-axis relative to the ambient sample position. This translation is the result of the particle velocity imparted to the sample by shock compression.[3,4] The net translation of the sample along the x-axis between the ambient and shock measurements is

$$t = t_{\text{shock}} + t_{\text{launch}} + t_{\text{pivot}}, \tag{6}$$

where t_{launch} was defined in Sec. II B.

The effect of the various lattice rotations and translations on the diffraction pattern is described next. Of particular interest is how the shock-induced changes to the diffraction pattern relate to shock-induced changes in the crystal microstructure, i.e., distributions in θ_1, $\delta\theta_{\text{mos,y}}$, and $\delta\theta_{\text{mos,z}}$. It is convenient to separate the discussion into horizontal changes to the diffraction pattern along x_d (primarily lattice compression) and vertical changes to the diffraction pattern along z_d (primarily lattice rotation).

1. Horizontal diffraction pattern changes

For the analysis of the horizontal changes, it is assumed that the incident beam is collimated vertically and that the reciprocal lattice vector under investigation does not have a z-component, i.e., $\delta\theta_{\text{tilt,y}}$ and $\delta\theta_{\text{m,y}}$ are both zero. With these assumptions the diffraction pattern will be at a height $z = z_d = 0$. The net horizontal shift of the diffraction peak on the detector between the ambient and shocked states is given by

$$x_d = R_d \tan[2(\theta_1 - \theta_0)] + x_{d,\text{tran}} + x_{d,\text{rot}}, \tag{7}$$

where

$$x_{d,\text{tran}} = 2t\cos\theta_1 \frac{\sin\theta_1}{\sin(\theta_1 - \delta\theta_{\text{m,z}})} \frac{\cos(\theta'_{1e} - \theta_0 + \delta\theta_{\text{m,z}})}{\cos(\theta'_{1e} + \theta_1 - 2\theta_0 + \delta\theta_{\text{m,z}})}$$
$$\times \{1 + \tan(\theta'_{1e} - \theta_0 + \delta\theta_{\text{m,z}})\} \tag{8}$$

and

$$x_{d,\text{rot}} = \left\{ R_d - R_s\cos[2(\theta_1 - \theta_0)] \frac{\sin(\theta_1 + \delta\theta_{\text{m,z}})}{\sin(\theta_1 - \delta\theta_{\text{m,z}})} \right\}$$
$$\times \frac{\sin(\theta'_{1e} - \theta_1 + \delta\theta_{\text{m,z}})}{\cos[2(\theta_1 - \theta_0)]\cos(\theta_1 + \theta'_{1e} - 2\theta_0 + \delta\theta_{\text{m,z}})}. \tag{9}$$

The first term in Eq. (7) is the relation between the Bragg angle shift and the diffraction peak shift on the detector for an ideally oriented, non-mosaic crystal. The term $x_{d,\text{tran}}$ is the shift on the detector due to the translation of the target, t, and is treated as a correction.[3,4] The term $x_{d,\text{rot}}$ is the shift on the detector that depends on the various lattice rotations

about the z-axis. For typical experiments, the translation correction $x_{d,tran}$ may be approximated as $2t\cos\theta_1$ and the shift due to rotations $x_{d,rot}$ may be neglected (provided $R_s = R_d$). However, if any of the various lattice rotation terms are not small, the full expressions (8) and (9) should be used in Eq. (7) when determining θ_1. Next, the effects of micro-lattice-strains and micro-lattice-rotations on the diffraction pattern are discussed.

If the crystal has a distribution of micro-lattice-strains along the loading direction (corresponding to a distribution in θ_1 values), then the Bragg condition will be satisfied in discrete locations over a finite horizontal width of the crystal. Each of the various locations on the crystal where the Bragg condition is satisfied has a particular value for the Bragg angle θ_1 that depends on the local longitudinal lattice strain. Different values of θ_1 result in diffracted x-rays at different positions x_d on the detector according to Eq. (7). Thus, provided that the lattice rotation term is small, a measure of the shock-induced horizontal broadening of the diffraction peak is related directly to the shock-induced distribution of micro-lattice-strains in the crystal.

If the crystal is mosaic and has a finite distribution of $\delta\theta_{mos,z}$ values, the Bragg condition will be satisfied in discrete regions of the crystal over a finite horizontal width; that width will grow with increasing $\delta\theta_{mos,z}$. However, the incident fan of x-rays covers a finite angular width and if the width of the distribution in $\delta\theta_{mos,z}$ becomes larger than $\Delta\theta_{inc}$, there will be crystallites with $\delta\theta_{mos,z}$ values on the tails of the mosaic distribution that do not contribute to the diffraction. Thus, when determining the width of the diffraction peak due to a distribution of $\delta\theta_{mos,z}$ values, the largest and smallest values of $\delta\theta_{mos,z}$ that should be used in Eq. (9) are $\Delta\theta_{inc}/2$ and $-\Delta\theta_{inc}/2$. In typical experiments, the effect of a distribution of $\delta\theta_{mos,z}$ values on the width of the diffraction peak is minimal so long as $R_d = R_s$. In other words, with the Bragg-Brentano parafocusing geometry the horizontal width of the peak is insensitive to micro-lattice-rotations. In some instances, it may be desirable to break the parafocusing geometry by focusing the incident beam directly on the sample ($R_s = 0$) in order to probe a small region of the crystal. In this case, a distribution of micro-lattice rotations $\delta\theta_{mos,z}$ causes a broadening of the peak that is roughly proportional to the width of the $\delta\theta_{mos,z}$ distribution (provided that the width of the distribution is less than $\Delta\theta_{inc}$). However, it is generally more convenient to examine micro-lattice-rotations by measuring the vertical height of the diffraction pattern as discussed next.

2. Vertical diffraction pattern changes

The position of the diffraction pattern relative to the ambient diffraction pattern is approximately given by

$$z_d = 2R_d \sin\theta_1(\delta\theta_{tilt,y} + \delta\theta_{mos,y}) \qquad (10)$$

for diffraction from a single mosaic block. A uniform lattice tilt ($\delta\theta_{tilt,y}$) due to the projectile tilt about the y-axis will shift the whole diffraction pattern vertically. The vertical position of the diffracted beam on the detector from each mosaic block will depend on the particular value of $\delta\theta_{mos,y}$ for a given block. Hence, the intensity of the diffracted beam as a

function of z_d is a direct measure of the distribution of micro-lattice rotations, $\delta\theta_{mos,y}$. The vertical position and height of the diffraction pattern on the detector is insensitive to micro-latttice strains.

V. REPRESENTATIVE DIFFRACTION RESULTS

A. Instrumental resolution

Figure 12 compares a diffraction pattern measured at the APS (Fig. 12(a)) with one measured using the flash x-ray
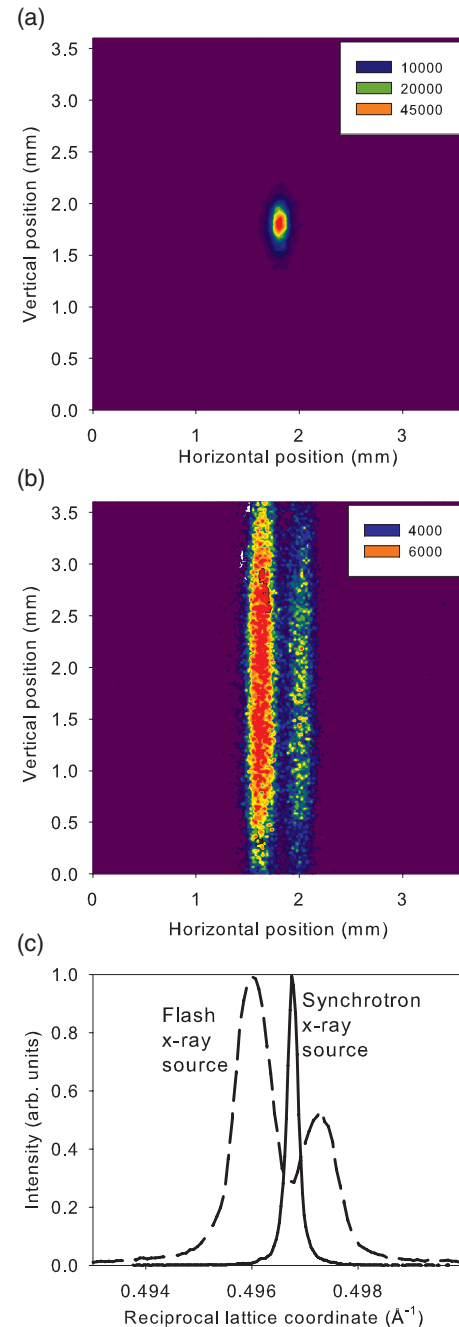

FIG. 12. (a) Diffraction image of a LiF 200 peak measured at the Advanced Photon Source. (b) Diffraction image of a LiF 200 peak measured using a flash x-ray source. (c) Comparison of horizontal cross sections of the LiF 200 peak in reciprocal space. The intensity scales of the diffraction images have arbitrary units.

system described in Ref. 4 (Fig. 12(b)). The conditions for the synchrotron measurement were as described in Sec. IV. For the flash x-ray measurements Cu Kα (8 keV) x-rays were used, $R_s = R_d = 186$ mm, and a vertical slit collimator was placed in front of the x-ray source. To compare the two measurements, horizontal cross sections are plotted vs. the reciprocal lattice coordinate in Fig. 12(c). The peak measured at the synchrotron is substantially narrower than the peak measured with the flash x-ray system. The small instrumental broadening at the synchrotron makes it easier to measure shock-induced broadening of the diffraction peak which can be related to micro-lattice strains as described in Sec. IV C. The resolution of the micro-lattice strain measurement at the APS is about 0.03% strain.

The height of the diffraction peak measured at the synchrotron for the ambient LiF crystal is primarily due to the height of the vertical beam at the detector and can, in principle, be made smaller by moving the vertical focus closer to the detector. In contrast, the height of the diffraction image using the flash x-ray system[4] is constrained only by the height of the sample unless horizontal x-ray slits are used. Even with horizontal slits, the diverging beam and large source height characteristic of a flash x-ray system make it more difficult to examine micro-lattice rotations than with a synchrotron x-ray source. The resolution of the micro-lattice-rotation measurement at the APS is about 0.02°.

B. Representative shock results

Typical diffraction patterns measured in a shock experiment at the APS are shown in Figure 13. The XRD geometry was as described in Sec. IV. The data in Fig. 13(a) are from a single pulse measurement of the 111 peak of Al(111) under ambient conditions with a Bragg angle of $\theta_0 = 17.55°$. The height of the diffraction peak is larger than that in the LiF sample in Fig. 12(a) which indicates that the Al(111) crystal has a distribution of micro-lattice rotations even in the ambient state. From the height of the peak, a full width at half maximum (FWHM) mosaic spread of about 0.1° was determined for the ambient Al(111) crystal. Although mosaicity increases the peak height above the height expected due to instrumental broadening alone, it does not cause significant horizontal broadening of the peak because of the parafocusing geometry.

The experimental arrangement for the shock experiment was as shown in Fig. 4. The Al6061 impactor had a velocity of 349 m/s. The target piece thicknesses were 2.018 mm, 0.819 mm, and 0.544 mm for the quartz, Al(111), and VC, respectively. The stress (1.7 GPa) and density compression ($\rho/\rho_0 - 1 = 0.021$) at the rear surface of the Al(111) were calculated using a one-dimensional wave propagation code.[27]

The diffraction pattern measured in the shocked state is shown in Fig. 13(b). It is shifted horizontally relative to the ambient peak. It is also somewhat taller and significantly broader than the ambient peak. The shift of the diffraction pattern corresponds to $\theta_1 - \theta_0 = 0.13°$ and the compression of the lattice planes along the loading direction is 0.73%. This lattice
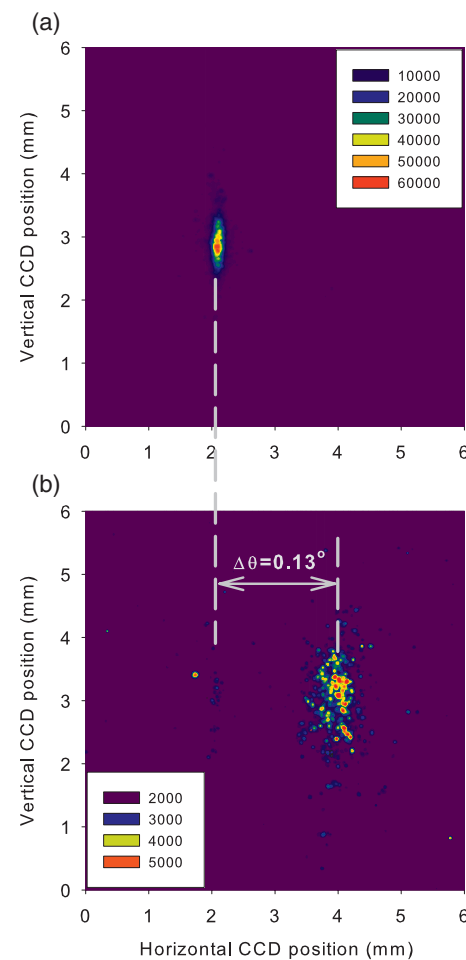

FIG. 13. Diffraction images of the 111 peak of an Al(111) sample. (a) Ambient diffraction pattern prior to shock loading. (b) Diffraction pattern measured in the shocked state showing a shift in the Bragg angle of 0.13°. The diffraction pattern from the shocked sample is taller and significantly broader than the diffraction pattern from the ambient sample. The intensity scales have arbitrary units.

compression is close to the lattice compression (0.69%) expected for a cubic unit cell with a density compression equal to the simulated value. Thus, as was found for LiF,[3,4] NaCl,[7] and Cu[14] crystals shocked along [100], the unit cell appears to be compressed nearly isotropically following shock compression.

The diffraction peak width in the shocked state is more than three times larger than the peak width in the ambient state. This increase in width corresponds to a 0.16% FWHM distribution of micro-lattice strains in the shocked state. The increase in the height of the diffraction pattern from the shocked crystal indicates that the mosaic spread increased from 0.1° to 0.24° as a result of shock compression.

Future shock compression experiments at the DCS, utilizing the Bragg-Brentano parafocusing geometry to examine microstructure of shocked single crystals, will have significantly better signal/noise than the data presented here due to nearly 100 times higher incident photon flux than used in the present work.

VI. CONCLUDING REMARKS

The experimental developments and the analysis procedures used at the APS to obtain high resolution x-ray diffraction measurements on shocked single crystals[19,20] were described. Two aspects of the work presented here are of particular significance for the DCS currently being developed at the APS: (1) synchronization/x-ray detection methods and (2) analysis equations for determining shocked crystal microstructure.

A significant experimental challenge in utilizing synchrotron x-rays for plate impact (shock-compression) experiments at the APS is the need to isolate x-ray signals generated from individual x-ray pulses arriving periodically at a shocked sample and at an area detector. A successful synchronization and x-ray detection approach utilizing an intensified charge-coupled device (ICCD) with a fast phosphor (Y_2SiO_5:Ce) was demonstrated. This synchronization method allowed us to obtain with certainty the diffraction signal from an x-ray pulse arriving at the sample during the desired uniaxial-strain, constant-stress time window. Recent impact work at the APS has demonstrated the ability to capture more than one frame by using a fast scintillator crystal and either multiplexing the signal to multiple ICCDs or using a framing CMOS camera.[22] By combining the approaches presented here and in Ref. 22, it will be possible to obtain multiple frames during a predetermined time window with certainty. However, further work is needed to optimize detectors and to develop faster x-ray shutters to limit the high heat loads imposed on the sample and detector elements when white beam and/or focused x-ray beams are used. An ideal shutter would have an insertion delay of a few microseconds or less and open times of a few microseconds or less. A possible approach would be to use a single shot explosive x-ray shutter triggered by an exploding bridge wire.

The synchrotron based Bragg-Brentano parafocusing approach for examining shocked crystals will be one of several types of x-ray measurement capabilities available at the DCS. Thus, the equations presented here for analyzing the shift and broadening of diffraction patterns for shocked single crystals will be useful for DCS users. Significant improvements over the present work are expected because the monochromatic flux incident on the sample at the DCS will be about 100 times larger than in the present work. An additional 100 times increase in flux will be possible by removing the double crystal monochromator and using the full pink beam. In that case, the diffracted beam in the horizontal direction will be broad due to the ∼5% bandwidth of the pink beam, but the vertical width of the diffraction pattern from the shocked crystal will still be dominated by lattice rotations. Hence, very precise measures of lattice rotation distribution in shocked single crystals will be possible in the future at the DCS.

ACKNOWLEDGMENTS

[1] Y. M. Gupta, Mater. Res. Soc. Symp. Proc. **538**, 139 (1999).

[2] Q. Johnson, A. C. Mitchell, and L. Evans, Appl. Phys. Lett. **21**, 29 (1972).

[3] P. A. Rigg and Y. M. Gupta, Appl. Phys. Lett. **73**, 1655 (1998).

[4] Y. M. Gupta, K. A. Zimmerman, P. A. Rigg, E. B. Zaretsky, D. M. Savage, and P. M. Bellamy, Rev. Sci. Instrum. **70**, 4008 (1999).

[5] T. d'Almeida and Y. M. Gupta, Phys. Rev. Lett. **85**, 330 (2000).

[6] P. A. Rigg and Y. M. Gupta, Phys. Rev. B **63**, 094112 (2001).

[7] E. Zaretsky, J. Appl. Phys. **93**, 2496 (2003).

[8] B. J. Jensen and Y. M. Gupta, J. Appl. Phys. **100**, 053512 (2006).

[9] S. J. Turneaure and Y. M. Gupta, Appl. Phys. Lett. **90**, 051905 (2007).

[10] S. J. Turneaure, Y. M. Gupta, and P. Rigg, J. Appl. Phys. **105**, 013544 (2009).

[11] S. J. Turneaure and Y. M. Gupta, J. Appl. Crystallogr. **44**, 574 (2011).

[12] S. J. Turneaure and Y. M. Gupta, J. Appl. Phys. **109**, 123510 (2011).

[13] S. J. Turneaure and Y. M. Gupta, J. Appl. Phys. **111**, 026101 (2012).

[14] A. Loveridge-Smith, A. Allen, J. Belak, T. Boehly, A. Hauer, B. Holian, D. Kalantar, G. Kyrala, R. W. Lee, P. Lomdahl, M. A. Meyers, D. Paisley, S. Pollaine, B. Remington, D. C. Swift, S. Weber, and J. S. Wark, Phys. Rev. Lett. **86**, 2349 (2001).

[15] D. H. Kalantar, J. F. Belak, G. W. Collins, J. D. Colvin, H. M. Davies, J. H. Eggert, T. C. Germann, J. Hawreliak, B. L. Holian, K. Kadau, P. S. Lomdahl, H. E. Lorenzana, M. A. Meyers, K. Rosolankova, M. S. Schneider, J. Sheppard, J. S. Stolken, and J. S Wark, Phys. Rev. Lett. **95**, 075502 (2005).

[16] J. Hawreliak, J. D. Colvin, J. H. Eggert, D. H. Kalantar, H. E. Lorenzana, J. S. Stolken, H. M. Davies, T. C. Germann, B. L. Holian, K. Kadau, P. S. Lomdahl, A. Higginbotham, K. Rosolankova, J. Sheppard, and J. S. Wark, Phys. Rev. B **74**, 184107 (2006).

[17] J. A. Hawreliak, D. H. Kalantar, J. S. Stolken, B. A. Remington, H. E. Lorenzana, and J. S. Wark, Phys. Rev. B **78**, 220101 (2008).

[18] M. Suggit, G. Kimminau, J. Hawreliak, B. Remington, N. Park, and J. Wark, Rev. Sci. Instrum. **81**, 083902 (2010).

[19] S. J. Turneaure, Y. M. Gupta, K. Zimmerman, K. Perkins, C. S. Yoo, and G. Shen, J. Appl. Phys. **105**, 053520 (2009).

[20] S. J. Turneaure and Y. M. Gupta, J. Appl. Phys. **106**, 033513 (2009).

[21] B. J. Jensen, S. N. Luo, D. E. Hooks, K. Fezzaa, K. J. Ramos, J. D. Yeager, K. Kwiatkowski, T. Shimada, and D. M. Dattelbaum, AIP Adv. **2**, 012170 (2012).

[22] S. N. Luo, B. J. Jensen, D. E. Hooks, K. Fezzaa, K. J. Ramos, J. D. Yeager, K. Kwiatkowski, and T. Shimada, Rev. Sci. Instrum. **83**, 073903 (2012).

[23] K. Ichiyanagi, S. Adachi, S. Nozawa, Y. Hironaka, K. G. Nakamura, T. Sato, A. Tomita, and S. Koshihara, Appl. Phys. Lett. **91**, 231918 (2007).

[24] *Phosphor Handbook*, edited by S. Shionoya and W. M. Yen (CRC, New York, 1999), p. 187.

[25] B. C. Stratton, R. Feder, S. von Goeler, G. F. Renda, V. J. Mastrocola, and J. L. Lowrance, Rev. Sci. Instrum. **75**, 3959 (2004).

[26] *International Tables for X-ray Crystallography*, edited by C. H. MacGillavry, G. D. Rieck, and K. Lonsdale (Kynoch, Birmingham, 1962), Vol. III, Chap. 3, Sec. 2.

[27] Y. M. Gupta, *COPS Wave Propagation Code* (Stanford Research Institute, Menlo Park, CA, 1978).